

Explanation of the anomalous redshift on nonlinear X-ray Compton scattering spectrum by a bound electron

SHANG SHI,^{1,7} JING CHEN,^{2,3} YUJUN YANG,⁴ ZHONG-CHAO YAN,^{5,6}
XIAOJUN LIU,⁶ BINGBING WANG,^{1,7,*}

¹Laboratory of Optical Physics, Beijing National Laboratory for Condensed Matter Physics, Institute of Physics, Chinese Academy of Sciences, Beijing 100190, China

²HEDPS, Center for Applied Physics and Technology, Peking University, Beijing 100871, China

³Institute of Applied Physics and Computational Mathematics, Beijing 100088, China

⁴Institute of Atomic and Molecular Physics, Jilin University, Changchun 130012, China

⁵Department of Physics, University of New Brunswick, Fredericton, New Brunswick, E3B 5A3, Canada

⁶State Key Laboratory of Magnetic Resonance and Atomic and Molecular Physics, Wuhan Institute of Physics and Mathematics, Innovation Academy for Precision Measurement Science and Technology, Chinese Academy of Sciences, Wuhan 430071, China

⁷University of Chinese Academy of Sciences, Beijing 100049, China

*wbb@aphy.iphy.ac.cn

Abstract: Nonlinear Compton scattering is an inelastic scattering process where a photon is emitted due to the interaction between an electron and an intense laser field. With the development of X-ray free-electron lasers, the intensity of X-ray laser is greatly enhanced, and the signal from X-ray nonlinear Compton scattering is no longer weak. Although the nonlinear Compton scattering by an initially free electron has been thoroughly investigated, the mechanism of nonrelativistic nonlinear Compton scattering of X-ray photons by bound electrons is unclear yet. Here, we present a frequency-domain formulation based on the nonperturbative quantum electrodynamic to study nonlinear Compton scattering of two photons off a bound electron inside an atom in a strong X-ray laser field. In contrast to previous theoretical works, our results clearly reveal the existence of anomalous redshift phenomenon observed experimentally by Fuchs *et al.* (Nat. Phys. **11**, 964 (2015)) and suggest its origin as the binding energy of the electron as well as the momentum transfer from incident photons to the electron during the scattering process. Our work builds a bridge between intense-laser atomic physics and Compton scattering process that can be used to study atomic structure and dynamics at high laser intensities.

© 2021 Optical Society of America under the terms of the [OSA Open Access Publishing Agreement](#)

1. Introduction

The Compton effect is well known for proving the quantum hypothesis of light in 1923 experimentally [1]. Afterwards the impulse approximation (IA) approach to Compton scattering on bound electrons, which considers the initial electron to be free with the momentum distribution of the bound state, was put forward by DuMond in his work on the scattering of photons from solids [2, 3]. Since the Compton profile is directly related to the electron momentum distribution, the electronic structure of atoms, molecules and solids can be probed by X- and γ -ray linear Compton scattering (LCS) [4–7] and analyzed by IA. For LCS process, Eisenberger and Platzman verified the validity of nonrelativistic IA for doubly differential cross sections [8], and later Ribberfors extended IA to relativistic region [9]. Modification of IA and reexamination of the validity of IA have been the main interests of recent studies [10–12].

With the first use of the Linac Coherent Light Source at the SLAC National Accelerator Laboratory in 2010 [13], the era of exploring the nonlinear interaction of ultrafast and ultra-intense X-rays with matters has begun. By using X-ray free-electron lasers [14–19], people

46 have observed for the first time extensive nonlinear phenomena at X-ray wavelengths, including
 47 the X-ray second harmonic generation in diamonds [20], two-photon absorption in the hard
 48 X-ray region [21, 22], electron femtosecond response to an ultra-intense X-ray radiation [23],
 49 and nonlinear Compton scattering (NCS) of X-ray photons [24]. Among them, the NCS is a
 50 particularly interesting phenomenon because the observed anomalous redshift of the scattered
 51 photon can be regarded as a breakdown of the widely-used IA theory for bound electrons.

52 As far as we know, there exist a few theoretical studies [25–27] devoted to the NCS processes
 53 involving bound electrons in recent years, but no theoretical work demonstrated the experimental
 54 observations by Fuchs *et al.* [24]. For example, Krebs *et al.* [26] developed a nonperturbative
 55 approach based on the time-dependent Schrödinger equation to investigate linear and nonlinear
 56 Compton scatterings of X-ray photons by atoms. However, their results were consistent with
 57 the predictions of the free-electron model and do not support the existence of the redshift found
 58 in [24]. More recently, Venkatesh and Robicieux [27] claimed that their theoretical results
 59 exhibit a blueshift compared with the scattered photon energy predicted by the free-electron
 60 model during an NCS process. Therefore, the origin of the anomalous redshift phenomenon
 61 observed by Fuchs *et al.* [24] is still an open question.

62 Motivated by the theoretical gap of the NCS mechanism, in this work we will apply the
 63 frequency-domain theory based on the nonperturbative quantum electrodynamic (QED) to study
 64 the NCS process of bound electrons. This theory has previously been successfully applied to
 65 recollision processes in strong laser fields [28–31]. The advantages of the QED method in
 66 treating the NCS could be shortly provided. Specifically, we will focus on the double differential
 67 probability (DDP) for the NCS process of a bound electron in an X-ray laser field. Our calculation
 68 will clearly demonstrate that in the DDP spectrum of the two-photon NCS, as the energy of the
 69 scattered photon increases, a redshift peak will appear, which is in contrast to the results by
 70 free-electron model [32–34], and other theoretical predictions [26, 27]. Our theoretical results
 71 can be considered as the first qualitative confirmation of the measurement of Fuchs *et al.* [24].

72 2. Frequency-domain theory of NCS by bound electrons

73 The frequency-domain theory is based on the nonperturbative quantum electrodynamic, where
 74 the laser-matter system can be regarded as an isolated one, hence the total energy of the system
 75 is conserved during the laser-matter interaction process and the formal scattering theory [35]
 76 can be applied. In this theory, the incident laser field, as a part of the whole system, is regarded
 77 as a quantized field, and all dynamic processes are treated as quantum transitions between two
 78 states of the laser-matter system. In the following, we develop this theory to investigate the NCS
 79 by a bound electron in intense laser fields. Natural units ($\hbar = c = 1$) are used throughout unless
 80 otherwise stated. The T -matrix element between the initial state $|\psi_i\rangle$ and the final state $|\psi_f\rangle$ is

$$T_{fi} = \langle \psi_f | V | \psi_i \rangle + \langle \psi_f | V \frac{1}{E_i - H_0 - U - V + i\epsilon} V | \psi_i \rangle, \quad (1)$$

81 where H_0 is the non-interaction part of the Hamiltonian for the atom-radiation system, U is the
 82 atomic binding potential, and V is the interaction operator between electron and photons. The
 83 initial state is $|\psi_i\rangle = \Phi_i(\mathbf{r}) \otimes |l\rangle \otimes |0\rangle$ with energy $E_i = (-E_B) + (l + \frac{1}{2})\omega_1 + \frac{1}{2}\omega_2$ for ω_1 the
 84 incident laser frequency and ω_2 the scattered photon frequency. Here, $\Phi_i(\mathbf{r})$ is the ground-state
 85 wave function of the atomic electron with the binding energy $E_B > 0$, and $|l\rangle$ and $|0\rangle$ are the
 86 Fock states of the incident and scattered photons with photon number l and 0, respectively. The
 87 final state is $|\psi_f\rangle = \Psi_{\mathbf{P}_f n_f} \otimes |1\rangle$ with total energy $E_f = \mathbf{P}_f^2 / (2m) + (n_f + \frac{1}{2} + u_p)\omega_1 + \frac{3}{2}\omega_2$,
 88 where $\Psi_{\mathbf{P}_f n_f}$ is the Volkov state of the electron in the incident laser field [28] with \mathbf{P}_f being the
 89 final momentum of the electron and u_p being the ponderomotive energy in unit of the incident
 90 photon energy.

91 The first and second terms in Eq. (1) correspond to a one-step and two-step transition,
 92 respectively. In this work, since the contribution of the two-step transition is much smaller than
 93 that of the one-step transition under the present laser conditions at the scattered photon energy
 94 around twice of the incident photon energy, the second term in Eq. (1) is dropped here and will
 95 be investigated in the future. Hence, the T -matrix element for NSC can be expressed as

$$T_{fi} = T_{AP} + T_{AA-} + T_{AA+}, \quad (2)$$

96 where $T_{AP} = \langle \psi_f | V_{22} | \psi_i \rangle$, $T_{AA-} = \langle \psi_f | V_{21-} | \psi_i \rangle$, and $T_{AA+} = \langle \psi_f | V_{21+} | \psi_i \rangle$. Here, the
 97 electron-photon interaction operators include $V_{22} = \frac{e}{m} g_2 e^{-i\mathbf{k}_2 \cdot \mathbf{r}} a_2^\dagger \boldsymbol{\epsilon}_2^* \cdot (-i\nabla)$, $V_{21-} = \frac{e^2}{m} g_1 g_2 \boldsymbol{\epsilon}_2^* \cdot$
 98 $\boldsymbol{\epsilon}_1 e^{i(\mathbf{k}_1 - \mathbf{k}_2) \cdot \mathbf{r}} a_1 a_2^\dagger$, and $V_{21+} = \frac{e^2}{m} g_1 g_2 \boldsymbol{\epsilon}_2^* \cdot \boldsymbol{\epsilon}_1^* e^{-i(\mathbf{k}_1 + \mathbf{k}_2) \cdot \mathbf{r}} a_1^\dagger a_2^\dagger$, where a_i (a_i^\dagger) being the annihilation
 99 (creation) operator and $g_i = (2\omega_i v_{\gamma_i})^{-\frac{1}{2}}$ with v_{γ_i} the normalization volume of the photon mode for
 100 $i = 1$ and 2 corresponding to the incident and scattered photon mode, respectively. \mathbf{k}_1 (\mathbf{k}_2)
 101 and $\boldsymbol{\epsilon}_1$ ($\boldsymbol{\epsilon}_2$) is the wave vector and polarization vector of the incident laser field (scattered photon
 102 mode), respectively.

103 Figure 1 illustrates the corresponding schematic diagrams of the three terms in Eq. (2), where
 104 we name T_{AP} the laser-assisted electron-mode (LEM) transition shown in Fig. 1(a), and name
 105 T_{AA-} and T_{AA+} the electron-assisted mode-mode (EMM) transitions shown in Fig. 1(b) and (c)
 106 respectively. The LEM transition describes the process where the bound electron is ionized after
 107 absorbing several photons from the laser field, and at the same time, a photon of frequency ω_2 is
 108 scattered, whereas the EMM transition describes a similar process except that a second photon
 109 of frequency ω_1 is either absorbed (T_{AA-}) or emitted (T_{AA+}).

110 The matrix element of the LEM transition T_{AP} can be written as

$$T_{AP} = \frac{e}{m} V_e^{-1/2} g_2 \boldsymbol{\epsilon}_2^* \cdot [\mathbf{P}_f + (u_p - q)\mathbf{k}_1] \mathcal{J}_q(\zeta, \eta) \\ \times \Phi_i(\mathbf{P}_f + \mathbf{k}_2 + (u_p - q)\mathbf{k}_1), \quad (3)$$

111 where $\mathcal{J}_q(\zeta, \eta) = \sum_{m=-\infty}^{\infty} J_{-q-2m}(\zeta) J_m(\eta)$ is the generalized Bessel function, with $\zeta = 2\sqrt{\frac{u_p}{m\omega_1}} \mathbf{P}_f \cdot$
 112 $\boldsymbol{\epsilon}_1$ and $\eta = u_p/2$. $q = l - n_f$ denotes the number of photons transferred from the incident laser
 113 field during the NCS process. The matrix elements of the EMM transitions $T_{AA\pm}$ are given by

$$T_{AA-} = \frac{e^2}{m} V_e^{-1/2} \Lambda g_2 \boldsymbol{\epsilon}_1 \cdot \boldsymbol{\epsilon}_2^* \mathcal{J}_{q-1}(\zeta, \eta) \\ \times \Phi_i(\mathbf{P}_f + \mathbf{k}_2 + (u_p - q)\mathbf{k}_1) \quad (4)$$

114 and

$$T_{AA+} = \frac{e^2}{m} V_e^{-1/2} \Lambda g_2 \boldsymbol{\epsilon}_1^* \cdot \boldsymbol{\epsilon}_2^* \mathcal{J}_{q+1}(\zeta, \eta) \\ \times \Phi_i(\mathbf{P}_f + \mathbf{k}_2 + (u_p - q)\mathbf{k}_1), \quad (5)$$

115 where $\Lambda = \sqrt{\frac{u_p \omega_1 m}{\alpha}}$ represents the half amplitude of the classical field in the limits of $g_1 \rightarrow 0$
 116 and $l \rightarrow \infty$. In Eq. (3)-(5), the two-photon NCS processes correspond to $q = 2$. Furthermore,
 117 the contribution of T_{AA+} can be ignored, since it is much smaller than that of the other two terms
 118 under the present laser conditions.

119 The expression of the DDP for a Compton scattering process can be written as [36]

$$\frac{dW_{i \rightarrow f}}{d\omega_2 d\Omega} = \int 2\pi |T_{fi}|^2 \delta(E_i - E_f) \frac{v_{\gamma_2}}{(2\pi)^3} \frac{V_e}{(2\pi)^3} \omega_2^2 d^3 P_f, \quad (6)$$

120 where $d\Omega$ is the differential solid angle of vector \mathbf{k}_2 . To analyze the results more clearly, we
 121 may rewrite the DDP by three parts:

$$\frac{dW_{i \rightarrow f}}{d\omega_2 d\Omega} = \frac{dW_{AP}}{d\omega_2 d\Omega} + \frac{dW_{AA}}{d\omega_2 d\Omega} + \frac{dW_{cro}}{d\omega_2 d\Omega}, \quad (7)$$

122 where the three parts on the right-hand of the equation represent the contributions of EMM,
 123 LEM and their cross-term (CT). In the following, we will see how these terms affect the peak
 124 position of the DDP spectrum for two-photon NCS processes.

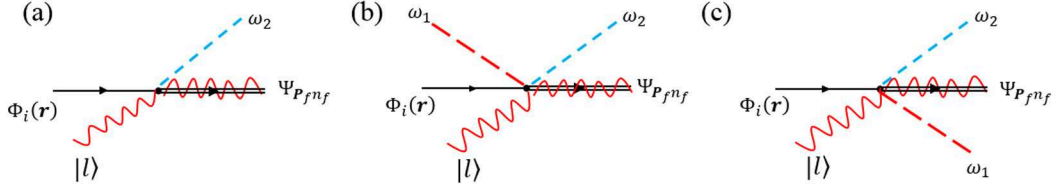


Fig. 1. Schematic for the one-step transition of Compton scattering by a bound electron. The single straight line represents the bound electron state, the wavy line represents the Fock state of the incident laser, the combination of wavy and double lines represents the Volkov state, the red and blue dashed lines represent the scattered photons of frequency ω_1 and ω_2 respectively, and the vertex denotes the transition operator V_{22} in (a), V_{21-} in (b), and V_{21+} in (c).

125 3. The redshift

126 We now calculate the DDP for two-photon Compton scattering by a $1s$ electron of Be atom,
 127 where the intensity of the laser field is 4×10^{20} W/cm² and the photon energy is 9.25 keV.
 128 Figure 2 presents the DDP of the NCS at the scattering angles of 45° (a), 90.5° (b) and 150°
 129 (c), where the wave vector of the scattered photon \mathbf{k}_2 is fixed in the polarization plane of the
 130 incident laser field defined by \mathbf{k}_1 (z -axis) and $\boldsymbol{\epsilon}_1$ (x -axis), i.e., the azimuthal angle $\phi = 0^\circ$. In
 131 Fig. 2(a)-(c), the vertical lines indicate the scattered photon energy predicted by the free-electron
 132 model [26, 27, 37]:

$$\omega_2 = \frac{q\omega_1}{1 + \frac{q\omega_1}{m}(1 - \cos\theta)}. \quad (8)$$

133 It can be seen from Fig. 2 that the peak positions on the scattered spectra at $\theta = 45^\circ$ and 150°
 134 are red shifted with respect to the scattered photon energy predicted by the free-electron model,
 135 while this peak position at $\theta = 90.5^\circ$ is blue shifted comparing with the scattered photon energy
 136 given by the free-electron model.

137 In order to explain the results shown in Fig. 2 (a)-(c), we present separately the contributions
 138 of LEM, EMM and CT by blue short-dotted lines (LEM), pink dash-dotted lines (EMM) and
 139 green dashed lines (CT) in Fig. 2(a)-(c). One may find that the EMM dominates the contribution
 140 to DDP at the scattered angle $\theta = 45^\circ$ and 150° as shown in Fig. 2(a) and (c), and hence the
 141 redshift of the peak on the DDP spectra can be attributed to EMM transition. On the contrary,
 142 LEM transition dominates the contribution to the DDP at $\theta = 90.5^\circ$, hence the blueshift of the
 143 peak on the DDP spectrum is due to LEM transition, as shown in Fig. 2(b). To find the reason
 144 of the shifts of these peaks, we may simplify Eqs. (3)-(4) by replacing the generalized Bessel
 145 functions $\mathcal{J}_2(\zeta, \eta)$ with $J_{-1}(\eta) + J_{-2}(\zeta) \approx C_1$ and $\mathcal{J}_1(\zeta, \eta)$ with $J_{-1}(\zeta) \approx C_2 \mathbf{P}_f \cdot \boldsymbol{\epsilon}_1$, because
 146 the values of ζ and η are much smaller than 1 under the present laser conditions. Here the
 147 parameters C_1 and C_2 are constants determined by the laser conditions. Therefore, the matrix

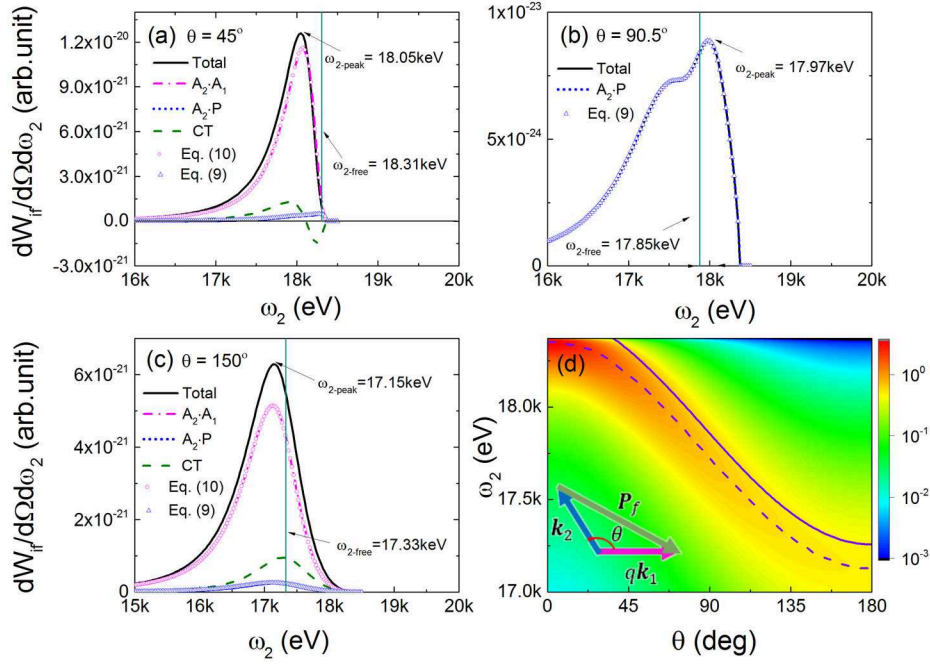


Fig. 2. The DDP as a function of the scattered photon energy ω_2 at the scattering angle of $\theta = 88^\circ$ (a), $\theta = 90.5^\circ$ (b) and $\theta = 150^\circ$ (c). The black solid lines represent the total DDP. The blue short-dotted lines, pink dash-dotted lines, and green dashed lines represent the DDP by LEM transition (Eq. (3)), the DDP by EMM transition (Eq. (4)) and the CT part of the total DDP, respectively. The blue triangles are for the DDP by Eq. (9) and the pink circles the DDP by Eq. (10). The vertical lines are ω_2 predicted by Eq. (8). The scattered wave vector \mathbf{k}_2 is fixed in the polarization plane defined by \mathbf{k}_1 and $\boldsymbol{\epsilon}_1$. (c) The integral of $|\Phi_i(\mathbf{P}_f + \mathbf{k}_2 + (u_p - q)\mathbf{k}_1)|^2$ over \mathbf{P}_f as a function of ω_2 and θ . The dashed line denotes the scattered photon energy corresponding to the peaks at different scattering angles and the solid line represents the prediction by Eq. (8).

148 element of LEM transition can be approximated as

$$T_{AP} \approx \frac{e}{m} V_e^{-1/2} g_2 (P_f \cos \theta_{\epsilon_2} - q \mathbf{k}_1 \cdot \boldsymbol{\epsilon}_2^*) \times C_1 \Phi_i(\mathbf{P}_f + \mathbf{k}_2 - q \mathbf{k}_1) \quad (9)$$

149 with θ_{ϵ_2} being the angle between $\boldsymbol{\epsilon}_2^*$ and the electron momentum \mathbf{P}_f . And the matrix element
150 of EMM transition can be approximated as

$$T_{AA-} \approx \frac{e^2}{m} V_e^{-1/2} \Lambda g_2 \boldsymbol{\epsilon}_1 \cdot \boldsymbol{\epsilon}_2^* P_f \cos \theta_{\epsilon_1} C_2 \times \Phi_i(\mathbf{P}_f + \mathbf{k}_2 - q \mathbf{k}_1) \quad (10)$$

151 with θ_{ϵ_1} being the angle between $\boldsymbol{\epsilon}_1$ and the electron momentum \mathbf{P}_f . The DDP spectra by
152 Eq. (9) and (10) are shown by the triangles and circles respectively in Fig. 2(a)-(c), where they
153 agree with the corresponding numerical results.

154 We firstly consider the influence of the atomic wavefunction on the DDP spectra. By integrat-
155 ing the modular square of the wavefunction over \mathbf{P}_f , we obtain the electron density distribution
156 as a function of the scattered photon energy ω_2 and the scattering angle θ , as shown in Fig. 2(d).
157 It shows that the peaks presented by dashed line on the density distribution decreases with the
158 scattering angle. This can be explained as follows: By analyzing the argument of the wavefunc-
159 tion, it can be found that the peak of the electron density distribution occurs at the momentum
160 transfer $\mathbf{P}_f = q \mathbf{k}_1 - \mathbf{k}_2$, as illustrated by the the inset of Fig. 2(d). Since this momentum transfer
161 increases with the scattering angle, the energy gained by electron from the scattering process in-
162 crease inevitably, leading to a decrease in the energy of the scattered photon. Moreover, one may
163 find that the peaks of the density distribution are always redshifted relative to the free-electron
164 model shown by the solid line, where the value of the redshift, in a range between 127 eV and
165 153 eV, is close to the binding energy of the 1s state of Be atom. This indicates that a bound
166 electron may provide a redshift on the peak of the DDP spectrum by its binding energy.

167 Next, to explain the redshift of the peaks on the spectra in Fig. 2(a) and (c) further, we find
168 from Eq. (10) that the DDP by EMM transition depends linearly on the value of the electron
169 momentum P_f . In particular, the value of P_f and thus the total DDP decrease as the scattered
170 photon energy increases due to the energy conservation. As a result, an obvious redshift of the
171 DDP spectrum is formed, which is mainly caused by the dependence of DDP on the ionized
172 electron momentum and bound-state wavefunction, as shown in Fig. 2(a) and (c). At last, to
173 understand the blueshift of the peaks on the DDP spectrum at $\theta = 90.5^\circ$ shown in Fig. 2(b), we
174 analyse Eq. (9) and find that the term $P_f \cos \theta_{\epsilon_2} - q \mathbf{k}_1 \cdot \boldsymbol{\epsilon}_2^*$ in Eq. (9) plays a crucial role on the
175 shift of the peaks, where the value of this term increases at around $\theta = 90^\circ$ with the scattered
176 photon energy, leading to the blueshift of peak on the DDP spectrum.

177 We then consider how the EMM and LEM transitions influence the total DDP for different
178 scattering angles. Fig. 3(a) presents the total DDP spectrum as a function of scattered photon
179 energy ω_2 and scattering angle θ at $\phi = 0^\circ$, where the dots show the peaks of the DDP spectra
180 and the solid lines predict the scattered photon energy by the free-electron model. One may find
181 that, except for a narrow region of the scattering angle around 90° , the peak value of the DDP
182 spectra decreases with the scattering angle and it is always red shifted relative to the scattered
183 photon energy of the free-electron model with a maximum redshift of 400 eV. Especially, the
184 peak at $\theta = 90^\circ$ is blue shifted comparing with the scattered photon energy by the free-electron
185 model. To explain these results, we present the DDP spectrum by EMM and LEM transitions in
186 Fig. 3(b) and (c), respectively. The dots in Fig. 3(b) and (c) show the peaks of the DDP spectra
187 and the solid lines show the prediction of the scattered photon energy by the free-electron model.
188 On the one hand, we may find that the the peaks of the DDP spectra by EMM decrease with the
189 scattering angle and is always red shifted comparing with the value of the free-electron model,

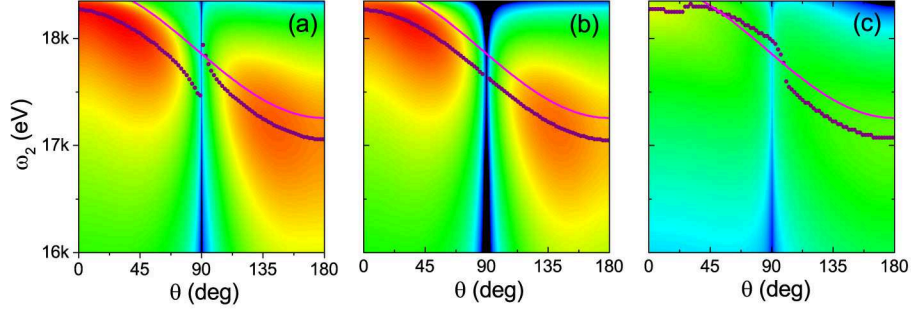


Fig. 3. Angle-resolved energy spectra of two-photon NCS by Be. The DDP is shown as a function of the scattering angle θ and the scattered photon energy ω_2 at $\phi = 0^\circ$. The total DDP, the DDP due to EMM, and the DDP due to LEM are shown in (a), (b) and (c), respectively. The solid lines represent ω_2 determined by Eq. (8). The dots denote the peaks at different scattering angles for the total DDP, the DDP of EMM term and the DDP of LEM term, respectively.

190 as shown in Fig. 3(b). In addition, the DDP spectrum of EMM transition presents a dip at
 191 about $\theta = 90^\circ$, which is also confirmed in Fig. 2(b). This is because that the DDP of EMM
 192 transition is proportional to $|\epsilon_1 \cdot \epsilon_2^*|^2$, which is zero at $\theta = 90^\circ$ due to the scattering geometry
 193 of $\epsilon_2 \perp \epsilon_1$ since $\mathbf{k}_2 \perp \mathbf{k}_1$ and $\mathbf{k}_2 \parallel \epsilon_1$. On the other hand, it can be found that the peaks of
 194 the DDP spectra by LEM presents a complex situation, where the peaks around $\theta = 90^\circ$ are
 195 blue shifted comparing with the prediction of the free-electron model and are red shifted at
 196 other scattering angles. Furthermore, comparing Fig. 3(a) with (b) and (c), we may find that
 197 the EMM transition dominates the contributions on the DDP spectrum, except for the region
 198 around $\theta = 90^\circ$ where the LEM dominates the total DDP spectrum. Therefore, the red shift of
 199 the peaks on the total DDP spectrum is attributed to the EMM transition, i.e., the dependence of
 200 DDP on the ionized electron momentum and bound-state wavefunction. Additionally, although
 201 the forward scattering is not given in the work of Fuchs *et al.* [24], our results show that the
 202 redshift phenomenon still exists significantly in the forward scattering.

203 We now qualitatively compare our NCS spectra with the experimental results [24] by using
 204 a magnification factor δ , where the DDP of two-photon NCS is shown in Fig. 4 at $\theta = 89^\circ$
 205 with $\delta = 2 \times 10^{16}$ (a) and $\theta = 117^\circ$ with $\delta = 1.11 \times 10^{14}$ (b). In Fig. 4(a)-(b), the curves
 206 and geometric symbols represent, respectively, the theoretical and experimental results under
 207 various laser intensities. Compared with the scattered photon energy predicted by free-electron
 208 model at $\theta = 89^\circ$ and $\theta = 117^\circ$, the peak energy obtained from our theory red shifts 393 eV and
 209 155 eV, respectively. Besides, it shows that the change of theoretical DDP with laser intensity
 210 agrees with the experimental results, which originates from the second-order nonlinear effects
 211 of laser intensity.

212 By integrating the DDP over the scattered photon energy, we obtain the corresponding single
 213 differential probability (SDP) shown in Fig. 4(c) and (d) with $\delta = 1.4 \times 10^{17}$ for the case of
 214 $\omega_1 = 8.84$ keV (c) and $\omega_1 = 9.75$ keV (d). It shows that the SDP increases as the scattering
 215 angle increases, which is in agreement with the experimental results displayed by the red stars in
 216 graphs. Moreover, the SDP from EMM and LEM transitions are also presented in Fig. 4(c) and
 217 (d). One may find that the SDP contributed by LEM transition is insensitive to the scattering
 218 angle, whereas the SDP by EMM transition increases with the scattering angle. Therefore,
 219 the dependence of the total SDP on the scattering angle can be mainly attributed to the EMM
 220 transition.

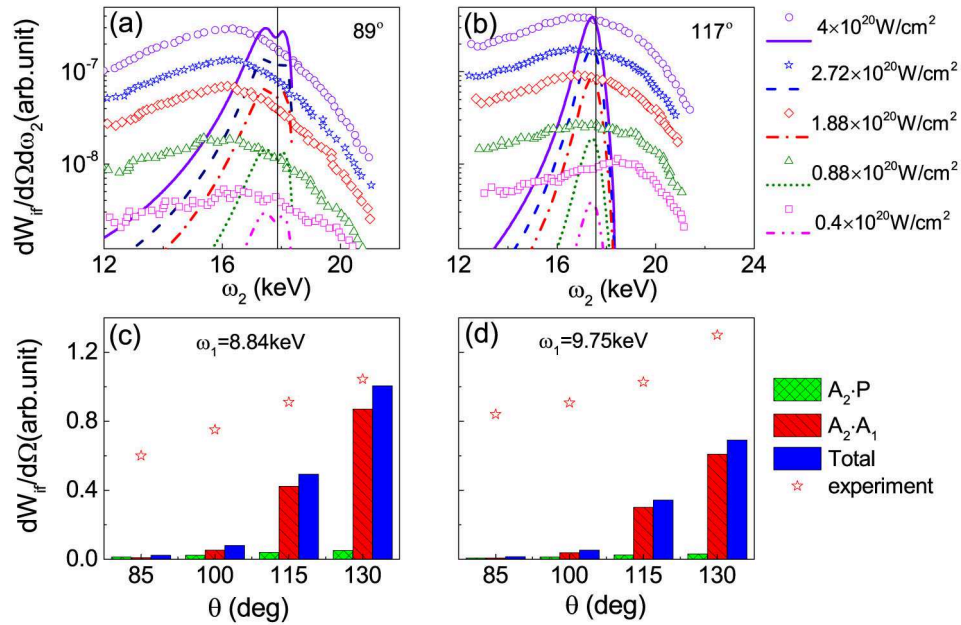


Fig. 4. Comparison between the DDP of theory and experiment. The DDP for two-photon NCS by Be at $\theta = 89^\circ$ (a) and $\theta = 117^\circ$ (b). The curves and geometric figures represent, respectively, the theoretical and experimental values under different laser intensities. The incident photon energy ω_1 is 9.25 keV. (c)-(d) Comparison of SDP between theory and experiment at different scattering angles at $\omega_1 = 8.84$ keV (c) and $\omega_1 = 9.75$ keV (d). The stars represent the experimental data points. Note: the theoretical values in the same graph are magnified by the same multiple.

221 4. Conclusion

222 We have extended the frequency-domain theory to investigate the NCS of two X-ray photons
 223 by an atom. Our theoretical results are in qualitative agreement with the experimental results
 224 of Ref. [24] and thus the underlying physical mechanism for the nonlinear scattering process,
 225 i.e., the observed anomalous redshifts are attributed to the atomic binding potential and the
 226 momentum transfer from the incident photons to the electron during the collision. Our results
 227 have demonstrated that the redshift can be observed in in both forward and backward directions.
 228 All these findings promote significantly the understanding of the nonlinear scattering processes
 229 of bound electrons in X-ray laser fields.

230 **Funding.** National Natural Science Foundation of China under Grant Nos. 12074418, 11774411 and
 231 11834015. ZCY was supported by the NSERC of Canada.

232 **Acknowledgments.** We thank all the members of SFAMP club for helpful discussions. S.S thanks D.
 233 Krebs and M. Fuchs for helpful discussions.

234 **Disclosures.** The authors declare no conflicts of interest.

235 **Data availability.** Data underlying the results presented in this paper are not publicly available at this
 236 time but may be obtained from the authors upon reasonable request.

237 References

238 1. A. H. Compton, "A quantum theory of the scattering of x-rays by light elements," Phys. review **21**, 483 (1923).

- 239 2. J. W. Du Mond, "Compton modified line structure and its relation to the electron theory of solid bodies," *Phys. Rev.*
240 **33**, 643 (1929).
- 241 3. J. W. DuMond, "The linear momenta of electrons in atoms and in solid bodies as revealed by x-ray scattering," *Rev.*
242 *Mod. Phys.* **5**, 1 (1933).
- 243 4. M. Cooper, "Compton scattering and electron momentum distributions," *Adv. Phys.* **20**, 453–491 (1971).
- 244 5. W. Ching and J. Callaway, "Band structure, cohesive energy, optical conductivity, and compton profile of lithium,"
245 *Phys. Rev. B* **9**, 5115 (1974).
- 246 6. D. Laurent, C. Wang, and J. Callaway, "Energy bands, compton profile, and optical conductivity of vanadium," *Phys.*
247 *Rev. B* **17**, 455 (1978).
- 248 7. P. Jaiswal and A. Shukla, "Kinetically balanced gaussian basis-set approach to relativistic compton profiles of atoms,"
249 *Phys. Rev. A* **75**, 022504 (2007).
- 250 8. P. Eisenberger and P. Platzman, "Compton scattering of x rays from bound electrons," *Phys. Rev. A* **2**, 415 (1970).
- 251 9. R. Ribberfors, "Relationship of the relativistic compton cross section to the momentum distribution of bound electron
252 states," *Phys. Rev. B* **12**, 2067 (1975).
- 253 10. V. Florescu and R. Pratt, "K-shell compton scattering at high photon energy," *Phys. Rev. A* **80**, 033421 (2009).
- 254 11. L. LaJohn, "Low-momentum-transfer nonrelativistic limit of the relativistic impulse approximation expression for
255 compton-scattering doubly differential cross sections and characterization of their relativistic contributions," *Phys.*
256 *Rev. A* **81**, 043404 (2010).
- 257 12. R. Pratt, L. LaJohn, V. Florescu, T. Surić, B. K. Chatterjee, and S. Roy, "Compton scattering revisited," *Radiat. Phys.*
258 *Chem.* **79**, 124–131 (2010).
- 259 13. P. Emma, R. Akre, J. Arthur, R. Bionta, C. Bostedt, J. Bozek, A. Brachmann, P. Bucksbaum, R. Coffee, F.-J. Decker
260 *et al.*, "First lasing and operation of an ångström-wavelength free-electron laser," *Nat. Photon.* **4**, 641–647 (2010).
- 261 14. R. Mitzner, B. Siemer, M. Neeb, T. Noll, F. Siewert, S. Roling, M. Rutkowski, A. Sorokin, M. Richter, P. Juranic *et al.*,
262 "Spatio-temporal coherence of free electron laser pulses in the soft x-ray regime," *Opt. express* **16**, 19909–19919
263 (2008).
- 264 15. B. W. McNeil and N. R. Thompson, "X-ray free-electron lasers," *Nat. Photon.* **4**, 814–821 (2010).
- 265 16. T. Ishikawa, H. Aoyagi, T. Asaka, Y. Asano, N. Azumi, T. Bizen, H. Ego, K. Fukami, T. Fukui, Y. Furukawa *et al.*,
266 "A compact x-ray free-electron laser emitting in the sub-ångström region," *Nat. Photon.* **6**, 540–544 (2012).
- 267 17. J. N. Galayda, J. Arthur, D. F. Ratner, and W. E. White, "X-ray free-electron lasers; present and future capabilities,"
268 *JOSA B* **27**, B106–B118 (2010).
- 269 18. P. R. Ribic and G. Margaritondo, "Status and prospects of x-ray free-electron lasers (x-fels): a simple presentation,"
270 *J. Phys. D: Appl. Phys.* **45**, 213001 (2012).
- 271 19. C. Bostedt, J. Bozek, P. Bucksbaum, R. Coffee, J. Hastings, Z. Huang, R. Lee, S. Schorb, J. Corlett, P. Denes *et al.*,
272 "Ultra-fast and ultra-intense x-ray sciences: first results from the linac coherent light source free-electron laser," *J.*
273 *Phys. B* **46**, 164003 (2013).
- 274 20. S. Shwartz, M. Fuchs, J. Hastings, Y. Inubushi, T. Ishikawa, T. Katayama, D. Reis, T. Sato, K. Tono, M. Yabashi
275 *et al.*, "X-ray second harmonic generation," *Phys. Rev. Lett.* **112**, 163901 (2014).
- 276 21. K. Tamasaku, E. Shigemasa, Y. Inubushi, T. Katayama, K. Sawada, H. Yumoto, H. Ohashi, H. Mimura, M. Yabashi,
277 K. Yamauchi *et al.*, "X-ray two-photon absorption competing against single and sequential multiphoton processes,"
278 *Nat. Photon.* **8**, 313–316 (2014).
- 279 22. S. Ghimire, M. Fuchs, J. Hastings, S. C. Herrmann, Y. Inubushi, J. Pines, S. Shwartz, M. Yabashi, and D. A. Reis,
280 "Nonsequential two-photon absorption from the k shell in solid zirconium," *Phys. Rev. A* **94**, 043418 (2016).
- 281 23. L. Young, E. P. Kanter, B. Kraessig, Y. Li, A. March, S. Pratt, R. Santra, S. Southworth, N. Rohringer, L. DiMauro
282 *et al.*, "Femtosecond electronic response of atoms to ultra-intense x-rays," *Nat. (London)* **466**, 56–61 (2010).
- 283 24. M. Fuchs, M. Trigo, J. Chen, S. Ghimire, S. Shwartz, M. Kozina, M. Jiang, T. Henighan, C. Bray, G. Ndashimiye
284 *et al.*, "Anomalous nonlinear x-ray compton scattering," *Nat. Phys.* **11**, 964–970 (2015).
- 285 25. A. N. Hoppersky, A. M. Nadolinsky, and S. A. Novikov, "Compton scattering of two x-ray photons by an atom," *Phys.*
286 *Rev. A* **92**, 052709 (2015).
- 287 26. D. Krebs, D. A. Reis, and R. Santra, "Time-dependent qed approach to x-ray nonlinear compton scattering," *Phys.*
288 *Rev. A* **99**, 022120 (2019).
- 289 27. A. Venkatesh and F. Robicheaux, "Simulation of nonlinear compton scattering from bound electrons," *Phys. Rev. A*
290 **101**, 013409 (2020).
- 291 28. D.-S. Guo, T. Åberg, and B. Crasemann, "Scattering theory of multiphoton ionization in strong fields," *Phys. Rev.*
292 *A* **40**, 4997 (1989).
- 293 29. L. Gao, X. Li, P. Fu, R. Freeman, and D.-S. Guo, "Nonperturbative quantum electrodynamics theory of high-order
294 harmonic generation," *Phys. Rev. A* **61**, 063407 (2000).
- 295 30. B. Wang, L. Gao, X. Li, D.-S. Guo, and P. Fu, "Frequency-domain theory of high-order above-threshold ionization
296 based on nonperturbative quantum electrodynamics," *Phys. Rev. A* **75**, 063419 (2007).
- 297 31. B. Wang, Y. Guo, J. Chen, Z.-C. Yan, and P. Fu, "Frequency-domain theory of nonsequential double ionization in
298 intense laser fields based on nonperturbative qed," *Phys. Rev. A* **85**, 023402 (2012).
- 299 32. F. Mackenroth and A. Di Piazza, "Nonlinear compton scattering in ultrashort laser pulses," *Phys. Rev. A* **83**, 032106
300 (2011).
- 301 33. D. Seipt and B. Kämpfer, "Nonlinear compton scattering of ultrashort intense laser pulses," *Phys. Rev. A* **83**, 022101

- 302 (2011).
- 303 34. A. Angioi, F. Mackenroth, and A. Di Piazza, "Nonlinear single Compton scattering of an electron wave packet,"
- 304 Phys. Rev. A **93**, 052102 (2016).
- 305 35. M. Gell-Mann and M. Goldberger, "The formal theory of scattering," Phys. Rev. **91**, 398 (1953).
- 306 36. R. Karzija, "Interaction between an atom and an electromagnetic field," in *Introduction to the Theory of X-ray*
- 307 *and Electronic Spectra of Free Atoms*, P. G. Burke, H. Kleinpoppen, R. B. Bernstein, J. C. Cohen-Tannoudji, R. W.
- 308 Crompton, Y. N. Demkov, C. J. Joachain, W. E. L. Jr., P.-. Löwdin, H. O. Lutz, M. C. Standage, and K. Takayanagi,
- 309 eds. (Plenum Press, 1996).
- 310 37. L. S. Brown and T. Kibble, "Interaction of intense laser beams with electrons," Phys. Rev. **133**, A705 (1964).